Journal of Applied Electrochemistry **34**: 997–1005, 2004.

High rate anodic dissolution of 100Cr6 steel in aqueous $NaNO_3$ solution

T. HAISCH[1]*, E.J. MITTEMEIJER[2] and J.W. SCHULTZE[3]
[1]*Robert Bosch GmbH, Schwieberdingen, Germany*
[2]*Max Planck Institute for Metals Research, Stuttgart, Germany*
[3]*Institut für Physikalische Chemie und Elektrochemie, Heinrich-Heine-Universität, Düsseldorf, Germany*
*(*author for correspondence, e-mail: tomhai@arcor.de)*

Received 25 March 2003; accepted in revised form 10 May 2004

Key words: anodic dissolution, current efficiency, electrochemical machining, oxygen evolution, passivation, polarization curves

Abstract

The high rate anodic dissolution of 100Cr6 steel in $NaNO_3$ electrolytes of various concentrations and at different temperatures was investigated. Galvanostatic flow channel experiments were used to examine the current efficiency of the steel substrate. Below 6 A cm^{-2} (zone A), oxygen evolution dominates, while at higher current densities iron dissolution prevails (zone C). Potentiodynamic polarization studies indicated a complete substrate surface passivation up to +1.8 V (vs NHE), and periodic fluctuations of the current density at higher anode potentials (> +1.8 V) due to severe oxygen evolution. Rotating cylinder measurements served for polarization studies at lower current densities in the region of dominating oxygen evolution. Scanning electron micrographs revealed a correlation between the current efficiency and the coverage of the substrate surface with an electronically conductive film at current densities of 2, 9 and 20 A cm^{-2}. The microstructure of the black, solid surface film developing during the high rate anodic dissolution of the steel was found to be heterogeneous and very porous. The main film components, as determined by X-ray diffraction and Auger electron spectroscopical measurements, were amorphous iron oxides, Fe_xO_y, and inert carbides, M_3C, originating from the steel matrix. An activation–repassivation process is proposed, which is responsible for the development of the complex multilayer (multiphase) structure observed at the steel substrate surface.

1. Introduction

The high rate electrochemical dissolution of iron and steels in sodium nitrate electrolytes has been the subject of a number of studies [1–7]. The results obtained from anodic polarization curves, current efficiency measurements and analysis of the resulting substrate surface morphologies show that $NaNO_3$ electrolytes have a passivating effect on iron-based substrates. It was found, that at low current densities ($i \leqslant 4$ A cm^{-2}) no metal is dissolved (current efficiency, $\eta = 0$). On this basis exact dimensional control can be achieved in the 'electrochemical machining' processes without mask techniques, such as holds for the fabrication of turbine engine parts, automotive components and electrochemical hole drilling [4–9].

It is well known, that the passivation of the substrate (anode) surface under conditions typical of ECM is due to complex anodic surface films developing at the substrate–electrolyte interface [10–17]. Several models for the development of these anodic surface film structures have been proposed. Usually a dual film structure is supposed: a hydrated oxide compound ($Fe_2O_3 \cdot H_2O$, FeOOH) film and a salt film precipitated from the $NaNO_3$ solution [4, 8, 17]. Due to the heterogeneous structure of a steel substrate, metal carbides influence the composition of the anodic surface film and thereby the polarization behaviour of the substrate [13–15]. Further, oxygen evolution at the anode surface has been observed as a competing reaction to metal dissolution [8, 14, 16, 18–24].

The purpose of this work is to investigate the mechanisms of metal dissolution, gas evolution and the solid surface film formation on the substrate of steel 100Cr6 in particular with a view to the intrinsic heterogeneity of the steel substrate.

2. Experimental details

Commercially obtained 100Cr6 steel specimens were used for the ECM experiments (rod material in soft annealed condition). The composition of the steel is as follows (in wt %): C 0.97; Cr 1.43; Si 0.28; Mn 0.28; Ni 0.11; P 0.006; S 0.002; Fe 96.92.

For the electrochemical dissolution experiments in the flow channel cell, a square electrode surface of 1 cm^2

was subjected to the flowing electrolyte. Platinized copper–tungsten alloy was used as cathode material. The set-up of the rectangular flow channel (parallel plate reactor) has been described elsewhere [13]. The average electrolyte flow velocity, u, was set at 7 m s^{-1} implying turbulent flow conditions. The distance between cathode and anode (working gap) was set at 2 mm. An aqueous $NaNO_3$ solution (40 wt %) at 40 °C ± 1 °C, pH 7, served as electrolyte. All experiments in the flow channel cell were performed *galvanostatically* with average current densities, i, in the range 5–60 A cm^{-2} (direct current). The specimens were subjected to electrochemical dissolution for 20 to 80 s.

All polarization measurements were carried out using an EG&G 273A potentiostat with simultaneous detection of the transferred charge, Q. 100Cr6 steel specimens (rings 12 mm dia., 0.5 mm height, with lateral area 0.19 cm^2) were applied as rotating cylinder electrodes (working electrodes, WE). A platinum net served as counter electrode (CE). A commercially obtained Ag/AgCl-electrode was used as reference electrode (RE). The distance between the working electrode and the counter electrode was set at 10 mm. Aqueous $NaNO_3$ solutions, at pH 7, of various concentrations and at different temperatures served as electrolytes. For the *potentiostatic* measurements, an anode potential of +2.5 V (vs NHE) was applied. *Potentiodynamic* curves were measured at 25 °C with a potential scan rate of 40 mV s^{-1} and anode rotation speeds of 590 and 1136 rpm (corresponding to Reynolds numbers $Re = \omega r^2/\nu = 1316$ and 2534, with $r^2 = 0.36$ cm^2 and $\nu_{25\,^\circ C} = 0.0169$ cm^2 s^{-1}; i.e., turbulent flow conditions).

For the *ex situ* scanning electron microscopy (SEM), X-ray diffraction and Auger electron spectroscopical (AES) investigations (Sections 4.2 and 4.3), the ECM-treated substrate was removed quickly from the reactor (flow channel cell or rotating cylinder electrode) and washed with distilled water. By this procedure, remainders of the $NaNO_3$ electrolyte were removed completely from the black surface film that was attached strongly to the steel specimen. Finally, the steel substrate was dried in a stream of nitrogen.

AES spectra were recorded with a PHI 600 Scanning Auger Microprobe. A sputter-depth profile (using Ar^+ ions of 3 keV for sputtering) was recorded over an area of 1 mm × 1 mm at an incidence angle of 60°. As a measure of the peak intensities the peak-to-peak height of the differentiated spectra was used. The sputter rate of 16 nm min^{-1} was calibrated using a Ta_2O_5-specimen as reference.

The X-ray diffraction analysis was performed with a Philips X'Pert diffractometer equipped with a Cu tube and a graphite monochromator in the diffracted beam to select Cu$K\alpha$ radiation. The diffracted intensity was recorded in the range 20–130° 2θ with a step size of 0.05° 2θ. All diffraction data required for interpretation of the X-ray diffraction patterns were taken from the JCPDS-International Centre for Diffraction data (PCPDFWIN database, version 2.01).

The current efficiencies of the galvanostatic flow channel experiments (Section 4.1) and the integral current efficiencies of the potentiodynamic measurements (Section 4.4) were calculated according to a procedure described elsewhere [14, 15].

3. Electrode reactions

3.1. *Anodic electrode reactions*

The principal ECM process is the divalent iron dissolution at the substrate–electrolyte interface according to Reaction 1. If additional, competing anodic reactions occur at the substrate surface (Reactions 2 and 3), current efficiencies $\eta < 100\%$ are observed.

$$Fe^0 \rightarrow Fe^{2+}_{aq} + 2e^- \quad \text{(divalent Fe dissolution)} \tag{1}$$

$$Fe^0 \rightarrow Fe^{3+}_{aq} + 3e^- \quad \text{(direct oxidation to Fe(+III))} \tag{2}$$

$$H_2O \rightarrow \frac{1}{2}O_2 + 2H^+ + 2e^- \quad \text{(oxygen formation)} \tag{3}$$

Generally these are the most important reactions [5–7]. For the case of armco-iron, current efficiencies of 66.6% indicate exclusive occurrence of Reaction 2 while high current efficiencies ($\eta \approx 100\%$) imply dominance of Reaction 1. Current efficiencies of about 100% have been observed for the case of NaCl electrolyte but not for $NaNO_3$ electrolyte [14]. For steel 100Cr6, the electroless removal (not dissolution) of corrosion resistant carbide particles causes an increase of η up to a maximum value of 116% in NaCl 15. Similarly, if metal dissolution occurs according to Reaction 2 a maximum current efficiency of 77% may be observed. If no metal dissolution occurs, oxygen evolution according to Reaction 3 dominates (Section 4.1).

3.2. *Cathodic electrode reactions*

Reactions, which are possible at the counter electrode surface are the reduction of nitrate, reduction of Fe(+III) and hydrogen gas evolution. Since cathodic gas evolution has not been observed in the present experiments (Section 4.4) it is proposed that the reduction of nitrate is the main reaction at the counter electrode upon ECM with $NaNO_3$ electrolyte.

3.3. *Electroless chemical reactions*

The electrochemical reactions given in Sections 3.1 and 3.2 are associated with charge flow at the electrode–

electrolyte interface. Electroless reactions are also possible, in particular with reference to the anodic processes. Since pronounced anodic oxygen evolution has been observed frequently in $NaNO_3$ systems [1, 2, 4–7], the O_2 bubble layer formation at the anode may be associated with electroless chemical oxidation of iron on the steel substrate surface.

3.4. *pH-shifts at the anode*

If oxygen evolution according to Reaction 3 occurs, a pH-shift within the anodic boundary layer from neutral to acid should be observed. According to the Pourbaix diagram for the system iron–water [25], a solid Fe_2O_3-film on the steel substrate would dissolve and release solvated Fe^{3+}-species at potentials above +0.77 V if the pH decreases to 0 and below. It should be recognized that the data presented in a Pourbaix diagram pertain to electrochemical equilibria, whereas in ECM processes nonequilibrium states occur which restricts the applicability of the Pourbaix diagram to ECM.

The rate determining steps of Reactions 1–3 consist of different elementary processes: the transfer of ions (ITR), electrons (ETR) or combined processes (CBR) [27]. Therefore, the rate of Reactions 1–3 depends on the oxide film thickness, the pH at the interface and the electrode potential in a complex way [26, 28].

4. Results and interpretation

4.1. *Current efficiency*

The current efficiency, η, for the dissolution of 100Cr6 steel in $NaNO_3$ (40 wt %) as a function of current density is shown in Figure 1. A typical roughly S-shaped curve can be observed [4–6, 14, 24]. Three different zones can be distinguished:

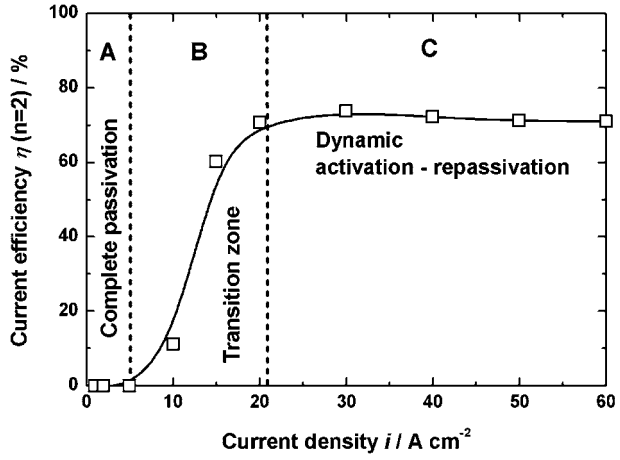

Fig. 1. Current efficiency (η) of the steel 100Cr6 (soft annealed) as observed in galvanostatic flow channel experiments ($NaNO_3$ (40 wt %), 7 m s^{-1}, 40 °C).

In zone A ($i \leqslant 6$ A cm^{-2}) a completely passivated substrate surface occurs: no metal dissolution takes place ($\eta = 0$). At this stage oxygen gas evolution is observed (Reaction 3). Consequently, the solution at the surface is acidified. The black solid surface film which develops during ECM is strongly attached to the steel substrate. The strong evolution of oxygen bubbles indicates good electronic conductivity of the surface film, due to the carbide particles (M_3C) or iron oxide (e.g., Fe_3O_4) in the surface film matrix.

The transition zone B (6 A cm^{-2} < i < 21 A cm^{-2}) is characterized by a steeply increasing current efficiency. Obviously, the reaction mechanism changes from one involving exclusive oxygen evolution to one that incorporates at least two competing anodic reactions, such as O_2 evolution and Fe^{n+} formation (Fe^{3+} according to the Pourbaix diagram) at the same time (note that the current efficiency has been calculated with respect to iron dissolution as Fe^{2+} (Reaction 1). Apart from trivalent iron dissolution, divalent iron dissolution according to Reaction 1 in combination with O_2 evolution may also be possible in nonequilibrium situations as in ECM, but no direct evidence is available.

Measurements in $NaNO_3$ in the pH range 3 to 8 at current densities below 10 A cm^{-2} gave similar results. This may be understood assuming that the surface pH is controlled by Reaction 3.

The highest current efficiencies occur in zone C ($i \geqslant 21$ A cm^{-2}). The observed value of η, of about 70%, might suggest dominant Fe^{3+} formation. However, at this stage part of the surface is still covered with a surface film (Section 4.2). Hence, Fe^{3+} formation, if it occurs, cannot be the only reaction at the anode. In an earlier study on ECM with steel, oxygen evolution was still observed at a current density of 47 A cm^{-2} [3]. The solid surface film is obviously ruptured at high current densities (Section 4.2). Partial film breakdown changes the nature of the solid surface film from compact and protective to porous and non-protective (Section 4.2).

4.2. *Anodic surface film structures/film breakdown*

SEM micrographs of solid surface films formed on soft annealed 100Cr6 substrates during ECM are shown in Figures 2(a)–(c). The surface films were obtained from galvanostatic flow channel experiments with aqueous $NaNO_3$ (40 wt %), at 7 m s^{-1}, 60 s, 40 °C.

The surface morphology as observed in zone A ($i = 2$ A cm^{-2}) is shown in Figure 2(a). The black, solid surface film is strongly attached to the steel substrate and covers the whole surface. It appears to be completely compact and only a few pores (ϕ < 1 μm) are observed (note that at the locations of nonmetallic inclusions, dark spots appear in the surface film). Local or global film breakdown does not occur.

In the transition zone B ($i = 9$ A cm^{-2}), two types of surface film structure coexist (Figure 2(b)): 'compact' regions, where the surface film is not ruptured (very similar to the surface film structure of zone A), and

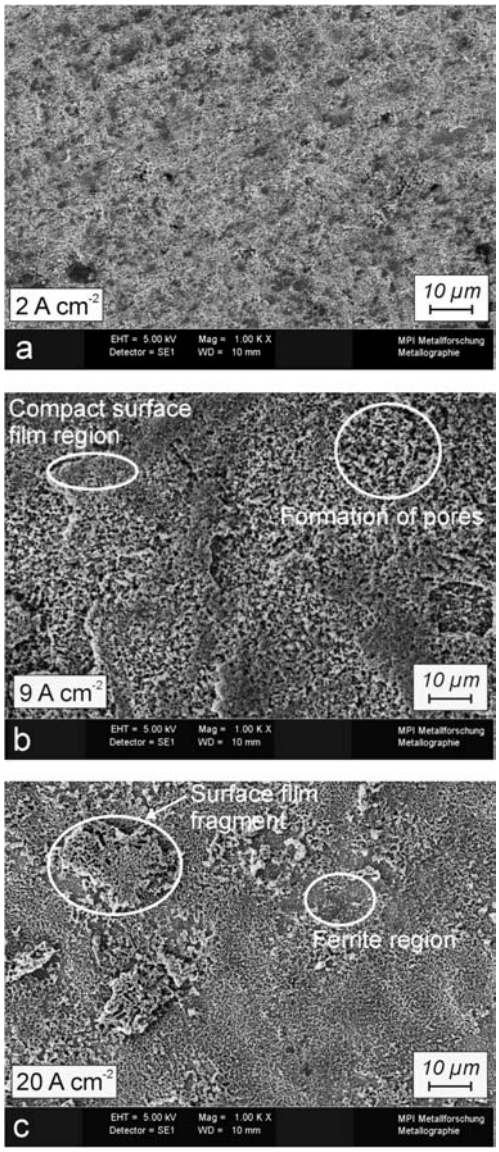

Fig. 2. SEM micrographs of solid surface films formed on soft annealed 100Cr6 substrates upon 'electrochemical machining' current density: (a) 2, (b) 9 and (c) 20 A cm^{-2}.

regions exhibiting massive formation of pores within the film. Regions on the substrate, where the complete anodic film structure has been detached, are not observed; the solid surface film is still strongly attached to the specimen. It may be assumed that Fe^{n+}-ions migrate preferentially through the pores. Then, within the pores the electrolyte is enriched in $Fe(NO_3)_3$ and becomes depleted of Na^+ [29].

In zone C ($i = 20$ A cm^{-2}), only a few single fragments of the surface film have remained on the steel substrate (Figure 2(c)). Most solid components of the film have been detached completely from the steel surface and large regions of the base substrate, that is without detectable surface film coverage, occur. Within the ferrite matrix of the substrate, carbides of composition M_3C (M = Fe, Cr) can be observed [14]. Even at higher current densities no clear electropolishing effects

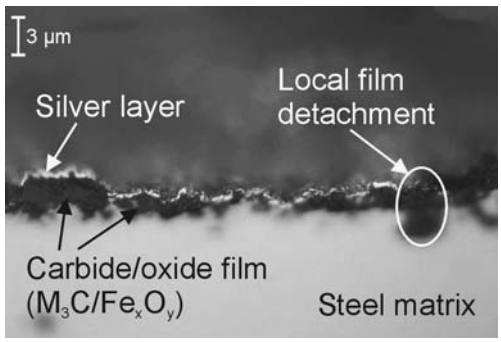

Fig. 3. Cross-sectional light optical micrograph (bright field) of a typical solid surface film formed on a 100Cr6 substrate during ECM (appears black in light microscopic investigation). Aqueous $NaNO_3$ (40 wt %), 10 A cm^{-2}, 60 s, 7 m s^{-1}, 40 °C.

were observed. It is assumed, that this observation is linked to the high Carbon content of the steel.

On the basis of the results presented in Figures 1 and 2, it is concluded, that compact surface films suppress active ferrite dissolution and promote oxygen evolution at the film–electrolyte interface.

A typical cross-section of a solid anodic surface film developed on a 100Cr6 substrate during ECM is shown in Figure 3 (zone B; parameters: flow channel cell, aqueous $NaNO_3$ (40 wt %), 10 A cm^{-2}, 60 s, 7 m s^{-1}, 40 °C). The surface film appears black, the steel matrix is grey. For better contrast, the surface film was covered with a 500 nm silver layer, which appears white in Figure 3. The thickness of the heterogeneous surface film varies extensively (0–3 μm).

4.3. *Surface film composition*

An AES sputter-depth profile of a surface film, formed on 100Cr6 in $NaNO_3$ (transition zone B, Section 4.2), is presented in Figure 4. After the removal of surface contamination during the first minutes of sputtering, large values for the C-content of the film were observed (~30 at %), indicating an enrichment of carbide particles at the substrate surface by the preferential dissolution of ferrite. After removal of ~1.6 μm film (100 min sputtering) the C-content had decreased from 30 to below 10 at % and approached the theoretical bulk value of 4.5 at %. AES-measurements of 100Cr6 steel substrates subjected to ECM in $NaNO_3$ for different reaction times (20–50 s) revealed the tendency of surface film thickening with increasing reaction time.

A substantial value for the atomic concentration of oxygen occurs within the anodic surface film, which is compatible with the presence of oxides as basic film components. The AES sputter-depth profiling does not allow determination of the composition of the oxide(s). Nitrogen was not found. In contrast to chloride-ions which can be intercalated and catalyse the film dissolution, the larger NO_3^--ions apparently cannot penetrate into the oxide film.

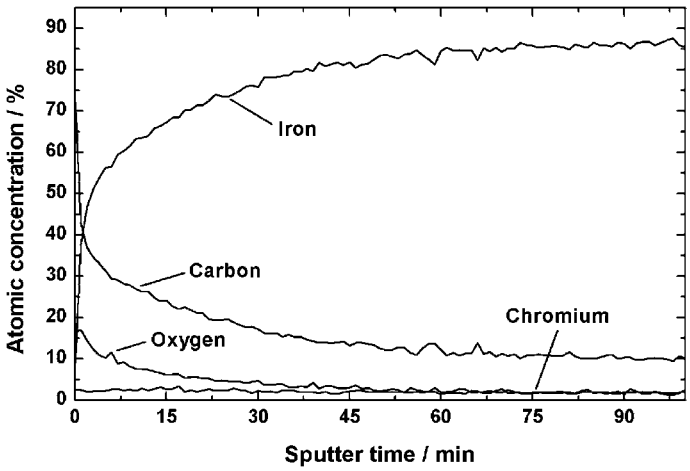

Fig. 4. Depth profile (Auger electron spectroscopy) of the solid surface film on a 100Cr6 substrate obtained from galvanostatic flow channel experiments. Parameters: aqueous $NaNO_3$ (20 wt %), 20 A cm^{-2}, 60 s, 7 m s^{-1}. Sputter rate, as indicated by sputtering a Ta_2O_5-reference specimen, is 16 nm min^{-1}.

X-ray diffraction patterns of a polished 100Cr6 reference specimen and of a 100Cr6 substrate after the ECM process with $NaNO_3$ are shown in Figure 5. The identified (and expected) components of the 100Cr6 reference (dotted line) are the α-iron matrix and carbides of composition M_3C (cementite type, see the enlarged parts of the diffraction patterns in Figure 5). The same components are observed for the substrate covered with the surface film, but the relative concentration of M_3C carbides appears larger (note the intensities of the M_3C peaks; the diffractional intensities were normalized with respect to the most intense α-iron peak occurring at $2\theta = 44.7°$). Diffraction peaks from iron oxides (Fe_xO_y) could not be clearly identified. It may be speculated that the peaks at $35° < 2\theta < 36°$ belong to iron oxides, but the measured intensities are too weak for unambiguous identification. This may indicate that the iron oxide(s) present in the surface film is (are) amorphous; oxygen was detected by AES. It may be suggested that a crystal lattice of an oxide cannot exist at very high ion current densities of $i > 10$ A cm^{-2}, which corresponds with a residence time of an iron-ion on a lattice position less than 100 μs.

4.4. *Polarization studies*

The potentiodynamic anodic polarization curves observed with 100Cr6 specimens applying the rotating cylinder electrode (RCE) were limited to current densities below 7 A cm^{-2}. The results indicate that active ferrite dissolution at low anode potentials does not occur in $NaNO_3$ electrolyte (Figure 6(a)). In contrast to typical activating ECM systems, which contain halide ions in the electrolyte [6, 13, 30], up to +1.8 V (vs NHE) no current flow is observed due to complete passivation of the steel surface. The existence of the passive region

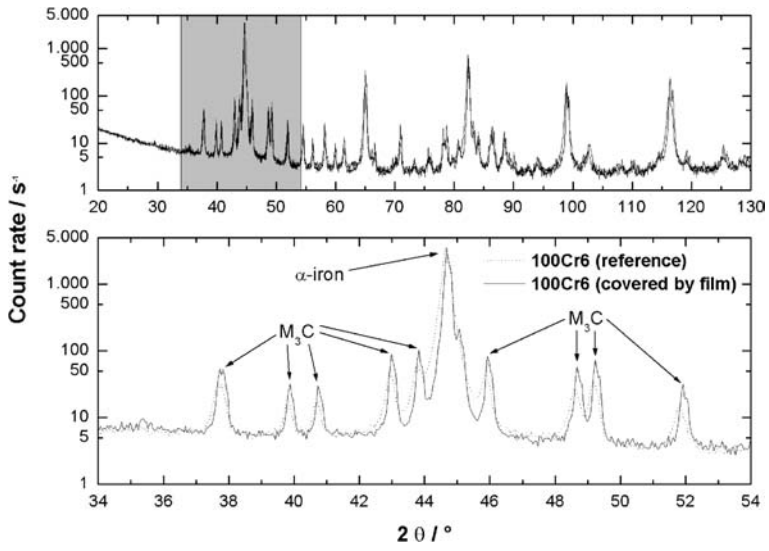

Fig. 5. X-ray analysis of a polished 100Cr6 reference in comparison with an ECM-treated substrate ($NaNO_3$ (20 wt %), 20 A cm^{-2}, 60 s, 7 m s^{-1}).

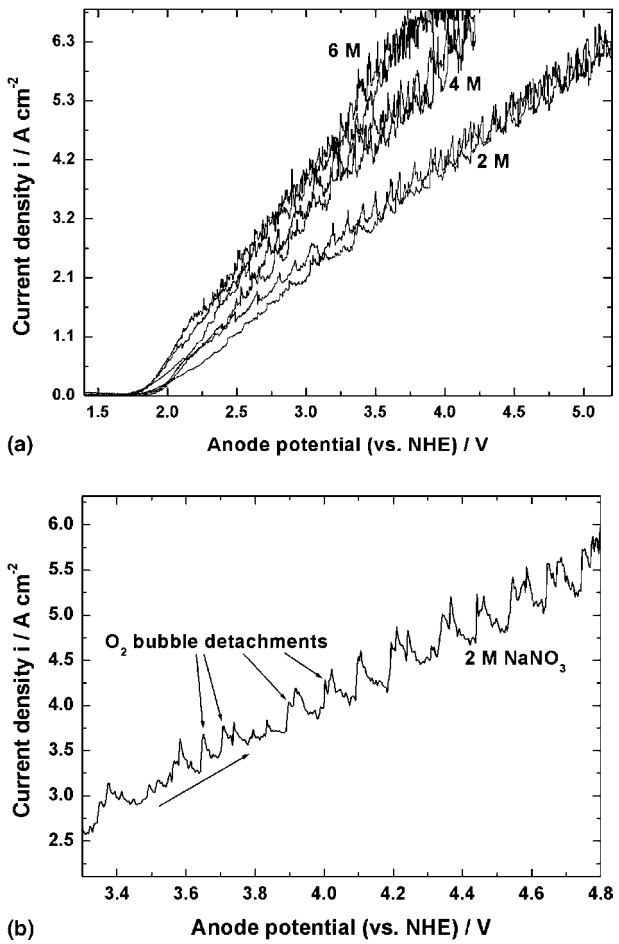

Fig. 6. (a) Anodic polarization curves of the steel 100Cr6 (soft annealed) in aqueous $NaNO_3$ of different concentrations (2, 4 and 6 M). Results obtained by potentiodynamic RCE-experiments. (Scan rate 40 mV s^{-1}; rotation speed 590 rpm; temperature 25 °C; cycles 1). (b) Enlarged part of the potentiodynamic polarization curve for 2 M $NaNO_3$ solution (Figure 6(a)).

was found not to depend on the concentration of the $NaNO_3$ electrolyte (Figure 6(a)). Obviously, nitrate ions in aqueous solutions are not able to activate the substrate surface at low potential [23, 24, 30]. The approximately linear behaviour of the polarization curves for anode potentials above +1.8 V is due to the onset of oxygen evolution, which is the main electrode reaction at low potential; it must be noted that a large IR error disturbs the curves. This is in accordance with integral current efficiencies $\eta < 25\%$ (calculated for Fe^{2+} dissolution), as determined for this potential range. Current efficiency values of the RCE experiments cannot be directly compared to those of the flow-channel-cell experiments: the current density during the RCE experiment varies, whereas that during the flow-channel-cell experiments is constant. For the calculation of RCE current efficiencies the total transferred charge $Q = I\mathrm{d}t$ and the weight loss of the substrate were measured. The polarization resistances, R_p, as determined from the slope, $\mathrm{d}U/\mathrm{d}i$, of the linear parts of the polarization curves, are 0.54 Ω cm^2 (2 M $NaNO_3$), 0.36 Ω cm^2 (4 M $NaNO_3$) and 0.29 Ω cm^2 (6 M $NaNO_3$). The relation of these polarization resistances to the corresponding separately measured conductivities of the $NaNO_3$ electrolyte (113 mS cm^{-1} (2 M), 160 mS cm^{-1} (4 M) and 176 mS cm^{-1} (6 M)) was found to be linear.

The O_2 bubble formation at the anode surface becomes obvious, when the periodic fluctuations superimposed on each polarization curve are recognized (Figure 6(b)). The enlarged part of the 2 M $NaNO_3$ polarization curve (forward scan) illustrates typical fluctuations in current density due to repeated O_2 bubble growth and detachment. At the points of steep upward 'jumps' of current density i, the detachment of an O_2 bubble collective, in association with local turbulence in the electrolyte, was observed by visual inspection of the anode surface. As a consequence, the resistance of the bubble layer, R_{gas}, drops to lower values.

Potentiostatic investigations, using the RCE without rotation, on passive film development occurring at the substrate surface at potentials lower than the oxygen evolution potential (+1.8 V; see above) are presented in Figure 7. The steel substrate was oxidized at four different anodic potentials. The time of the anodic period was chosen such that the current density had approximately reached the limiting current density of 23.6 mA cm^{-2} (dotted line in Figure 7). After anodization, a fast switch to the cathodic potential of −0.5 V (vs NHE) was carried out to demonstrate that reduction of the passive film then takes place (stars in Figure 7). The charges required for establishing complete film reduction to Fe^0 were found to be 19 mC (at +1.2 V), 23 mC (+1.4 V), 37 mC (+1.6 V) and 56 mC (+1.8 V). Assuming that a compact Fe_2O_3 film with a density of 5.24 g cm^{-3} [33] had developed on the substrate and that no charge had been carried by cathodic nitrate reduction, the thicknesses of the passive films were calculated from the values of transferred charges as

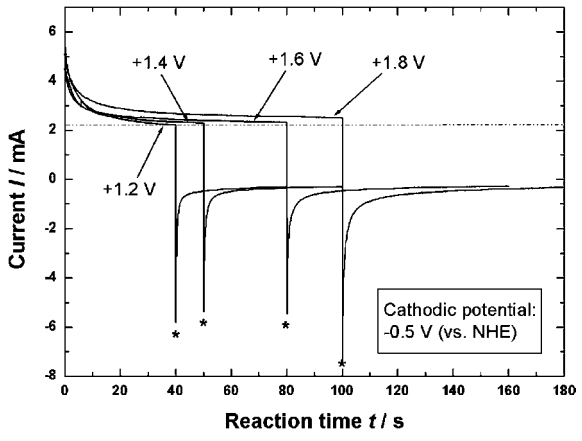

Fig. 7. Potentiostatic measurements of anodic passive film growth and cathodic film reduction (anode surface 0.094 cm^2). The potentials for anodic polarization are given in the Figure, the cathodic reduction potential for all single measurements was −0.5 V (vs NHE). The points of the anodic/cathodic potential switches are indicated by stars in the figure. Steel 100Cr6, $NaNO_3$ (40 wt %), 25 °C, no electrode rotation or electrolyte flow.

102 nm (+1.2 V), 124 nm (+1.4 V), 203 nm (+1.6 V) and 309 nm (+1.8 V). These thickness values are significantly higher than those reported for armco-iron substrates [18], due to the fact that the anodic charges transferred in the present experiments are many times larger. Additionally, the presence of carbides in 100Cr6 provokes layer thickening.

4.5. *Influence of temperature*

The temperature dependence of the anodic polarization curves of 100Cr6 in $NaNO_3$ (40 wt %) was investigated in region A up to the beginning of region B. The measurements show that the passivation region (0 to +1.8 V) exists at all temperatures investigated (10–70 °C). No clear tendency for the temperature dependence of the anodic polarization curves was found for the potential region above +1.8 V; the shapes of the curves are similar to those presented in Figure 6(a). The polarization curves are the outcome of competing iron dissolution and oxygen evolution. A possible variation in relative contributions of these reactions during the potentiodynamic measurement complicates the interpretation of the polarization curves. Mass loss measurements were carried out to demonstrate the temperature dependence of the integral current efficiency; calculated for a dissolution valence $n = 2$ (Figure 8). The result reveals, that with increasing electrolyte temperature, oxygen evolution at the substrate surface is significantly enhanced and iron dissolution is suppressed.

The results presented in Figures 6(a) and 8 are consistent with polarization measurements at varying electrode rotation speeds, which showed a very small dependence on the hydrodynamic conditions in the ECM system in the region of dominating oxygen evolution ($i < 5$ A cm^{-2}) [14]: since ferrite dissolution is only a side reaction in $NaNO_3$ electrolytes at low anode potentials, ECM is not rate controlled by the Fe^{n+}-diffusion from the electrode surface, and therefore no limiting current density, i_{lim}, depending on the electrode rotation speed, occurs in the polarization curves (Figure 6(a)). The situation changes at high current densities where the role of iron dissolution becomes more important: an oversaturated film may be formed and the transport by diffusion and migration of Fe^{n+} will be dominant [29].

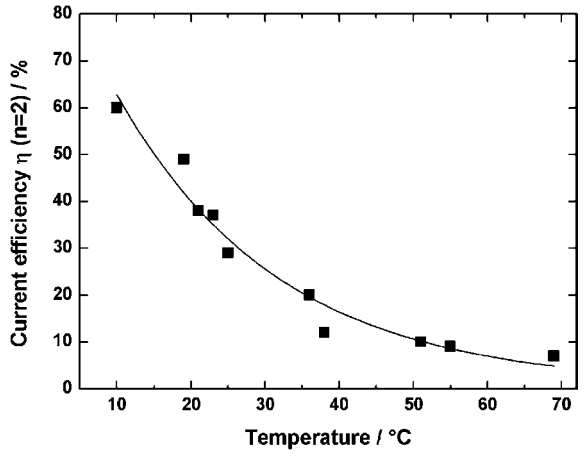

Fig. 8. Temperature dependence of integral current efficiency for divalent iron dissolution, obtained by potentiodynamic RCE-experiments (100Cr6, $NaNO_3$ (40 wt %); scan rate 40 mV s^{-1}; rotation speed 1136 rpm; potential scan range +0.22 V to +4.22 V (vs NHE), cycles 1).

5. A model description for ECM with $NaNO_3$ electrolytes

In general, solid surface films develop during high rate electrochemical dissolution of iron and steels when passivating electrolytes like $NaNO_3$, Na_2SO_4 and Na_3PO_4 are applied in ECM [1–7, 10, 11, 13–21, 23, 24, 30, 31]. For the case of steel substrates in passivating electrolytes, very heterogeneous and irregular anodic surface film structures develop, dependent on the current density, the electrolyte composition, the temperature and the substrate microstructure [14, 15]. For this reason, several different mechanisms of surface film growth and breakdown have been proposed [17, 30].

It is usually suggested, in particular for chloride containing electrolytes, that anodic film breakdown is caused by penetration of (Cl^-)-anions into the developing film, dominantly composed of Fe_xO_y. Anions in the film at weak spots, for example, at dislocations or at the interface with inclusions originating from the steel matrix, initiate film rupture. The number of incorporated anions increases with increasing potential [17, 30]. If the ability of the anion to penetrate the protective surface film is not strong enough, as in the case of $NaNO_3$ electrolytes where the size of NO_3^--ions is larger than that of Cl^--ions, the above picture is inadequate.

A possible model for ECM in $NaNO_3$ electrolytes is presented in Figure 9. A soft annealed steel substrate containing globular carbides M_3C (black spots) within the ferrite matrix (α-iron, grey) is subjected to high rate electrochemical metal dissolution. At low potentials (< +1.8 V) extremely low current densities occur due to the formation of very thin passive films (Figure 7). If electrochemical equilibrium is established these passive films have the composition Fe_2O_3 in the potential range −0.1 V to +1.8 V, at pH 7 [25, 32]. If the potential is increased to +1.8 V and above the current density increases significantly but the current efficiency is still

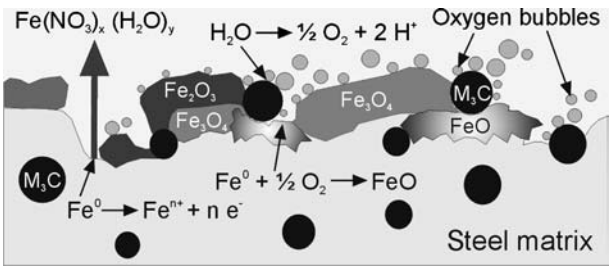

Fig. 9. A model description for ECM of the soft annealed steel 100Cr6 in $NaNO_3$. The steel matrix contains globular carbides (M_3C, black) surrounded by ferrite (grey).

zero (zone A; Figures 1 and 6). In zone A, oxygen evolution occurs exclusively. The dissolution of ferrite becomes increasingly important in zone B. The relatively thick solid surface film is composed of iron oxides and metal carbides (Figures 4 and 5). FeO may initially be an important component [34]. In any case this oxide is unstable under ECM conditions and further oxidation may occur. The initial appearance of an amorphous structure for the iron oxide may be understood recognizing the very short residence time of the iron ion on a single lattice site of the order of 10^{-4} s at a current density of 10 A cm^{-2}. This suggests that there may not be enough time to form a crystal lattice. The formation of magnetite and haematite on iron has been reported [4, 10, 11]. Carbide particles in the steel matrix are inert and are incorporated in the developing film. Pores and holes at the interfaces with the carbides may be filled efficiently by, in particular, the amorphous iron oxide component, thereby giving good adhesion of the carbides. As a result, a highly heterogeneous film structure is formed by diverse oxide components and inert carbide particles. As both the solid oxidation product Fe_3O_4 (dark grey, Figure 9) and the insoluble carbides M_3C are nearly metallic conductive [15, 26], oxygen evolution is expected along the entire film surface. The acidification of the solution due to Reaction 3 is expected to be greater around the carbides.

Since the transport of Fe^{n+}-ions by migration and diffusion through solid surface film components is slow as compared to electron transport, oxygen evolution increases with increasing substrate surface coverage. Oxygen evolution occurs exclusively at the film surface; at the bare metal surface ferrite dissolution is favoured. Recognizing that oxygen evolution can also occur within pores in the heterogeneous film structure, it is conceivable that the mechanical stress within the surface film increases and this may be the main cause of local film rupture at the location of single pores as observed in the experiments. Progress of film rupture leads to areas where large scale film detachment occurs. This then is a metal dissolution activating process. Furthermore, acidification as a consequence of anodic O_2-development leads to iron oxide dissolution and thereby film thinning, facilitating surface film rupture/detachment.

Copious oxygen bubble formation may allow subsequent repassivation of the activated metal surface regions. Thus, the highly heterogeneous surface film structure observed as a function of current density is the result of a dynamic process of activation and repassivation. In turbulent flow conditions it is possible that, in addition to the metal removal by a diffusion/migration, a considerable amount of metal removal is realized by mechanical erosion by solid metal carbides M_3C from the anode surface [13]. Since the mechanical erosion process requires the presence of solid particles in the flowing liquid which impact the surface film [13], it follows, that once the surface film is locally damaged and becomes thinner due to dissolution as a consequence of local acidification, the mechanical erosion process becomes increasingly severe. Hence, the average thickness of the developing solid surface film is determined by competing processes of electrochemical surface film growth and film thinning by the electroless mechanical erosion of solid components in the turbulent liquid (Fe_xO_y, $Fe(OH)_x$, FeO(OH), M_3C) and/or the dissolution of the iron oxide structure.

6. Conclusions

1. Description of the electrochemical metal dissolution in $NaNO_3$ ECM-systems requires recognition of at least three competing anodic reactions, which may occur simultaneously: Fe^{2+}-, Fe^{3+}-formation and O_2-evolution (also [16]).
2. Complete passivation of the steel (100Cr6) substrate surface corresponding to the presence of a black surface film is established for anode potentials up to +1.8 V (vs NHE).
3. At low current densities, above the threshold potential of +1.8 V (vs NHE), exclusive oxygen evolution is observed (zone A). The electronically conductive surface film covers the entire substrate surface. Periodic overall current density fluctuations observed in the polarization measurements indicate the formation-detachment-process of oxygen bubble groups at the anode surface. Oxygen evolution is associated with acidification of the boundary layer.
4. With increasing current density and decreasing electrolyte temperature the formation of Fe^{n+} species is enhanced, while oxygen evolution diminishes (zones B and C).
5. Electrochemical Fe^{n+} dissolution becomes the dominating ECM-reaction, if pronounced detachment of the surface film occurs. This situation prevails at high current densities ($i > 20$ A cm^{-2}).
6. The black, solid surface film which develops on a 100Cr6 substrate upon ECM is constituted of amorphous Fe_xO_y components and inert M_3C carbides, originating from the steel matrix, which have become embedded by the heterogeneous oxide matrix.
7. ECM of 100Cr6 steel in $NaNO_3$ can be conceived as an activation–repassivation process. The initial, compact anodic surface film on the steel substrate is locally ruptured at high current densities due to the development of oxygen gas in the pores of the film in association with film thinning as a consequence of acidification. As a result, bare metal substrate surface may occur on a microscopic scale. Subsequently, the development of a new surface film on the bare metal surface causes repassivation.

References

1. K.-W. Mao, *J. Electrochem. Soc.* **118** (1971) 1876.
2. K.-W. Mao, *J. Electrochem. Soc.* **120** (1973) 1056.
3. D.-T. Chin and A.J. Wallace, *J. Electrochem. Soc.* **120** (1973) 1487.

4. D.-T. Chin and K.-W. Mao, *J. Appl. Electrochem.* **4** (1974) 155.
5. J.A. McGeough, 'Principles of Electrochemical Machining', (Chapman & Hall, London, 1974).
6. M. Datta, *IBM J. Res. Develop.* **37** (1993) 207.
7. M. Datta, *IBM J. Res. Develop.* **42** (1998) 655.
8. M. Datta and D. Landolt, *Electrochim. Acta* **25** (1980) 1263.
9. D. Landolt, R.H. Muller and C.W. Tobias, *J. Electrochem. Soc.* **116** (1969) 1384.
10. M. Nagayama and M. Cohen, *J. Electrochem. Soc.* **109** (1962) 781.
11. M. Nagayama and M. Cohen, *J. Electrochem. Soc.* **110** (1963) 670.
12. J.P. Hoare and C.R. Wiese, *Corros. Sci.* **15** (1975) 435.
13. T. Haisch, E.J. Mittemeijer and J.W. Schultze, *Z. Metallkd.* **92** (2001) 417.
14. T. Haisch, E.J. Mittemeijer and J.W. Schultze, *Electrochim. Acta* **47** (2001) 235.
15. T. Haisch, E.J. Mittemeijer and J.W. Schultze, *Mater. Corros.* **53** (2002) 740.
16. K.-W. Mao, M.A. LaBoda and J.P. Hoare, *J. Electrochem. Soc.* **119** (1972) 419.
17. T.P. Hoar, *Corros. Sci.* **7** (1967) 341.
18. M. Datta, H.J. Mathieu and D. Landolt, *J. Electrochem. Soc.* **131** (1984) 2484.
19. M. Datta and D. Landolt, *J. Electrochem. Soc.* **122** (1975) 1466.
20. M. Datta and D. Landolt, *J. Electrochem. Soc.* **124** (1977) 483.
21. M. Datta and D. Landolt, *J. Appl. Electrochem.* **7** (1977) 247.
22. L. Franke and W. Forker, *Electrochim. Acta* **19** (1974) 27.
23. A.D. Davydov, E.Y. Grodzinski and A.N. Kamkin, *Elektrokhimiya* **9** (1973) 518.
24. A.D. Davydov and V.D. Kaschtschejev, *Elektrokhimiya* **9** (1974) 154.
25. M. Pourbaix, 'Atlas of Electrochemical Equilibria', 1st English edn (Pergamon Press, Oxford 1966).
26. U. Stimming and J.W. Schultze, *Electrochim. Acta* **24** (1979) 859.
27. J.W. Schultze and M.A. Habib, *J. Appl. Electrochem.* **9** (1979) 255.
28. J.W. Schultze and M.M. Lohrengel, *Electrochim. Acta* **45** (2000) 2499.
29. M.M. Lohrengel, paper presented at the ISE-Meeting in Düsseldorf (2002).
30. A.D. Davydov, *Elektrokhimiya* **14** (1978) 979.
31. K. Chikamori and S. Ito, *Denki Kagaku* **39** (1971) 493.
32. B. Beverskog and I. Puigdomenech, *Corros. Sci.* **38** (1996) 2121.
33. R.C. Weast and M.J. Astle, 'Handbook of Chemistry and Physics', 60th edn (CRC Press, Baco Ratton, FA, 1979–1980).
34. A.M. Sukhotin and K.M. Kartashova, *Corros. Sci.* **5** (1965) 393.